Journal of Materials Chemistry C

PAPER

View Article Online
View Journal | View Issue

Cite this: J. Mater. Chem. C, 2014, 2, 9385

Conjugation of TEM-EDX and optical spectroscopy tools for the localization of Yb^{3+}, Er^{3+} and Co^{2+} dopants in laser glass ceramics composed of $MgAl_2O_4$ spinel nano-crystals embedded in SiO_2 glass

G. Boulon,*[a] G. Alombert-Goget,[a] Y. Guyot,[a] M. Guzik,[ab] T. Epicier,[c] N. P. Blanchard,[a] L. Chen,[d] L. Hu[d] and W. Chen[d]

Received 24th June 2014
Accepted 6th August 2014

DOI: 10.1039/c4tc01344a

www.rsc.org/MaterialsC

The main goal of this work is to conjugate two independent techniques of TEM-EDX and optical spectroscopy, which is rare, for the localization of Yb^{3+} and Er^{3+} rare earth ions and Co^{2+} transition metal ions as dopants in a compact self-Q-switched microchip laser glass ceramic composed of $MgAl_2O_4$ spinel nano-crystals of 10–20 nm size embedded in SiO_2 glass. The use of the TEM-EDX technique associated with both the elemental mapping of each dopant and the direct visualization of the heavier rare earth ions has led to the result that Er^{3+} and Yb^{3+} rare earth ions are preferentially located in the spinel nano-crystals. Regarding the low Co^{2+} concentration this technique was not accurate enough for characterization and finally we have used absorption spectroscopy to probe the main presence of Co^{2+} ions in the spinel nano-crystals. The use of Yb^{3+} ions as structural probes allows the identification of the 0-phonon broad line at 977 nm as both that of the disordered glass and that of the spinel inverted phases. A new Yb^{3+} radiationless center has been pointed out by the presence of a strong absorption line at 970 nm which has been assigned to the strongly perturbed area of the spinel nano-crystallite surface. This dopant characterization is worthwhile to be shown as a special case where characterization of rare earth and transition metal ions needs the use of both TEM and spectroscopic techniques.

1. Introduction

Passively Q-switched, diode-pumped solid state lasers are currently being used as miniature or micro-lasers capable of delivering a high peak output power at high repetition rates and a short nanosecond (ns) temporal pulse width. These lasers are of great interest due to their potential applications in micro-machining, remote sensing, targeting, ranging, and microsurgery. Cr^{4+} and Co^{2+} dopants have been proposed as saturable absorbers for passive Q-switching of solid-state lasers operating in the near-infrared region. Most commonly, systems presently used are based on Nd^{3+}:YAG or Nd^{3+}:YVO_4 lasers, passively Q-switched by Cr^{4+}:YAG, where the unique well-known characteristics of Cr^{4+} garnets as saturable absorbers are applied.[1–4] Another crystal like Cr^{4+}:Mg_2SiO_4 was also proposed as a saturable absorber.[5] The most important application of the oxide crystals doped with tetrahedrally coordinated Co^{2+} ions is passive Q-switching of solid-state lasers operating in the near-infrared region. A number of crystals such as YAG, $LaMgAl_{11}O_{19}$ (LMA), and ZnSe were doped with Co^{2+} ions.[6,7] As an example, the passively Q-switched 1.34 μm Nd^{3+}:$Y_xGd_{1-x}VO_4$ laser with a Co^{2+}:$LaMgAl_{11}O_{19}$ saturable absorber was demonstrated.[8]

The original idea was proposed recently with transparent glass ceramics[9,10] containing Yb^{3+}, Er^{3+} ions in a glass matrix and Co^{2+}-doped $MgAl_2O_4$ nano-crystals of sizes of 10–20 nm, which can be used as a compact self-Q-switched microchip laser. Indeed, glasses containing nano-crystals embedded in a glass matrix can enhance existing or offer completely new properties compared to those of the precursor glass. These transparent glass ceramics possess the spectral requirements of both eye safe lasers by Er^{3+} $^4I_{13/2} \rightarrow {}^4I_{15/2}$ emission in the glass matrix between 1.5 and 1.6 μm under Yb^{3+} pumping and saturable absorbers by $^4A_2$ (F) → $^4T_1$ (F) transition of Co^{2+}-doped $MgAl_2O_4$ nano-crystals so that, together, might be developed as a self-Q-switched microchip laser. A previous analysis has shown that Yb^{3+} and Er^{3+} seem to remain in the SiO_2 glass

[a]Institute Light Matter (ILM), UMR5306 CNRS-University Lyon1, University of Lyon, Bât. Kastler, 69622 Villeurbanne, France. E-mail: georges.boulon@univ-lyon1.fr
[b]Faculty of Chemistry, University of Wroclaw, 14 Joliot-Curie, PL-50-383 Wroclaw, Poland
[c]MATEIS, UMR 5510 CNRS-INSA of Lyon, University of Lyon, Bât. Pascal, 69621 Villeurbanne, France
[d]High Power Laser Components R&D Center, Shanghai Institute of Optics and Fine Mechanics, Chinese Academy of Sciences, Jiading, Shanghai 201800, China

matrix, while Co^{2+} occupies the tetrahedral sites in $MgAl_2O_4$ nano-crystals.[10]

The main goal of this study is to report deeper complementary spectroscopic measurements to solve more accurately the problem of the location of dopants in the two glassy and nano-spinel phases in order to check the feasibility of this laser system.

2. Experimental techniques

2.1. Sample preparation

Glass with a composition (in wt%) of $1.8Yb_2O_3$–$1.7Er_2O_3$–$11MgO$–$31.5Al_2O_3$–$47SiO_2$–$4.5TiO_2$–$2.5ZrO_2$–$0.03CoO$ (CYE glass) was prepared, where TiO_2 and ZrO_2 were used as mixed nucleating agents.[10] Concentrations of Co^{2+}, Yb^{3+} and Er^{3+} ions are 5.77×10^{18} cm^{-3}, 1.5×10^{20} cm^{-3}, and 1.46×10^{20} cm^{-3}, respectively. For comparison, CoO-undoped glass (YE glass) with the same composition was also prepared. For the two glasses, homogeneous mixtures (300 g) of analytical reagent grade raw materials, obtained by ball milling, were melted in a corundum crucible in a laboratory electric furnace at 1580 °C for 4 h in an air atmosphere under stirring. According to differential scanning calorimetry (DSC) analysis, CYE and YE glass samples were heat treated at 760 °C for 12 h, and then at 930 °C for 4 h. As a result, transparent CYE GC and YE GC were synthesized. The purity of Yb_2O_3 and Er_2O_3 is 4N, while other reagents are of analytical grade.

For comparative absorption analysis of samples containing different concentrations of Yb^{3+} and one Er^{3+} concentration we used the compositions (in wt%) of $2Yb_2Er$, $4Yb_2Er$, and $6Yb_2Er$, it means xYb_2O_3–$1.1Er_2O_3$–$(3.3 - x)La_2O_3$–$11MgO$–$30.6Al_2O_3$–$47SiO_2$–$4.5TiO_2$–$2.5ZrO_2$–$0.03CoO$ ($x = 1.1$, 2.2, 3.3), respectively.

2.2. Experimental section

2.2.1. TEM-EDX experiments. Experiments were conducted on the Cs-corrected TITAN Environmental Transmission Electron Microscope (ETEM) from FEI installed at CLYM (Centre Lyonnais de Microscopie, http://www.clym.fr) and operating at 300 kV. Thin foils were prepared by ion bombardment (PIPS system from GATAN). According to this preparation method, some Ar has been detected during EDX analysis with a SDD analyzer from Oxford Instruments (classical implantation of Ar^+ ions in glassy phases). Cu is also detected as a spurious element due to the sample environment in the microscope. During TEM work, irradiation effects were encountered due to the high electron flux at 300 kV. However, all reported observations were obtained in reasonably short times and prior to any significant degradation (*e.g.* drift, deformation or detectable structural chemical variation), unless otherwise specified. Especially, chemical analysis in EDX was limited to reduced doses and short acquisition times, thus limiting the signal-to-noise ratio and the sensitivity of the measurements to detect the very small concentrations of Yb^{3+}, Er^{3+}, and Co^{2+} dopants. Under these conditions, both the detection limit and the accuracy of the present results are estimated to be about 0.2 at% for all species of special interest, *i.e.* the doping ions Yb^{3+}, Er^{3+} and Co^{2+}. Nanoprobe analysis and EDX elementary maps in the Scanning TEM (STEM) mode were performed using a probe of about 2 to 4 nanometers (full-width at half-maximum). Micrographs were acquired in both Cs-corrected high resolution and high angle, annular dark field (HAADF) STEM modes.

2.2.2. XRD experiments. A Rigaku Ultima IV X-ray diffractometer with Cu Kα radiation was used to measure the diffraction angle 2theta ranging from 10° to 80°.

2.2.3. Absorption spectroscopy. Absorption spectra in the 200–2500 nm spectral range were recorded at 4 and 293 K with a Cary-Varian 5000 Scan spectrometer equipped with an Oxford CF 1204 helium flow cryostat. A special thin layer technique was used to detect the 4f → 4f transitions.

The homogenous and well-ground nano-powder of spinels was compressed in the form of pellets under 20 MPa pressure. Very thick and transparent samples prepared in this way were used for the absorption measurements.

2.2.4. Luminescence spectroscopy. Emission measurements under pulsed laser excitation (OPO laser, EKSPLA NT342, 10 Hz, 7 ns) were performed with the help of a cooled germanium cell (NORTHCOAST) coupled to a boxcar SRS250. For the comparative measurements of the integral intensity a CW titanium sapphire laser coupled with a IR Hamamatsu CCD camera with a 900 l mm^{-1} grating blazed at 1300 nm was used. The emission spectra were recorded both at room as well as at liquid nitrogen temperature.

The luminescence decay curves were recorded under pulsed laser excitation (OPO laser, EKSPLA NT342, 10 Hz, 7 ns) and detection of the fluorescence intensity around 1.06 μm was possible with the help of a fast cooled germanium cell (NORTHCOAST) coupled to a LECROY LT 342 digital oscilloscope. The luminescence decay curves were recorded at room and liquid nitrogen temperatures.

3. Results and discussion

3.1. Morphology of samples observed by TEM measurements

A typical STEM-HAADF image is presented in Fig. 1a where spinel nanoparticles appear with a brighter contrast with respect to the vitreous matrix. Their size ranges typically between 4 and 20 nm with an average at around 10 nm. Lattice imaging clearly indicates the crystalline nature of the spinel phase as shown in Fig. 2.

Crystallographic indexing was performed either in the conventional diffraction mode or by using Fourier transforms, or diffractograms, of the HREM images as reported as an inset in Fig. 2: all acquired data are fully consistent with the usual spinel, the $Fd\bar{3}m$ structure of $MgAl_2O_4$ with $a = 0.808$ nm. A confirmation of this finding is presented in Fig. 3 where a spinel crystallite is observed at high resolution in the [001] viewing direction.

The *d*-spacing and growth direction of the nanoparticles have been indexed and presented in Fig. 2 and 3.

This is important to evaluate the ratio between the $MgAl_2O_4$ nano-spinel crystallites and the SiO_2 glassy phase. To do so,

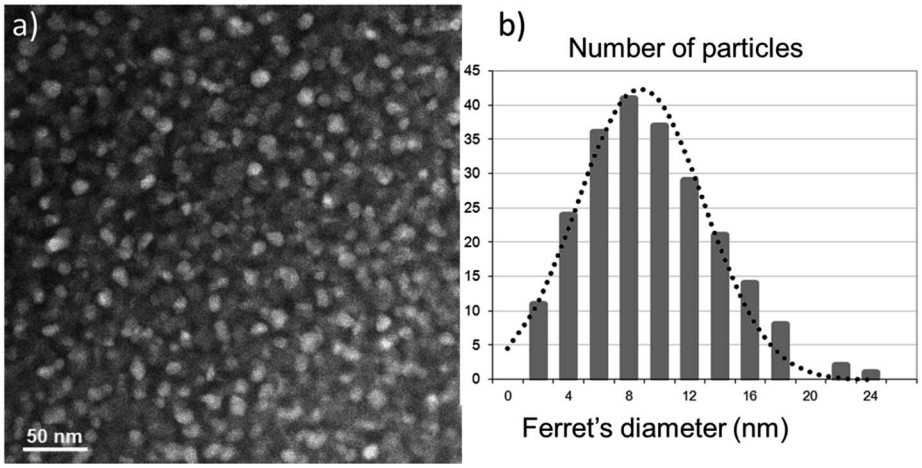

Fig. 1 (a) Typical STEM-HAADF image showing the distribution of spinel nanocrystallites embedded in the silicate glassy phase (spinel nanoparticles appear with a brighter contrast with respect to the vitreous matrix). (b) Size histogram of the micrograph shown in (a); a mean equivalent (Ferret's) diameter of 10 ± 0.3 nm can be deduced from a Gaussian fit (dotted curve).

EDX results obtained on large areas of about 1 μm^2 were fitted by a linear combination of the expected chemical formula of both phases: $xMgAl_2O_4 + (1 - x)SiO_2$, where x represents the atomic fraction of the spinel phase. According to the usual consideration of absorption effects, linked to the sample thickness (estimated here to about 50 nm, with little incidence on the final spinel fraction in the interval 0–100 nm), the elemental contents for the major constituents O, Mg, Al, and Si were deduced from the experimental and the spinel atomic fraction x was refined from a simple mean-least square fitting procedure (see Fig. 4): using this approach, an optimum value of $x = 25\%$ was found.

3.2. Distribution of Yb^{3+}, Er^{3+}, and Co^{2+} dopants as revealed by nano-probe EDX

One main challenge of the present structural characterization is to know not only the distribution of Yb^{3+}, Er^{3+}, and Co^{2+} dopants in both glassy and crystalline phases, but also at the interface between the nano-spinel crystals and the glass. The greatest difficulty when applying the TEM-EDX technique is to find out adequate thin regions where no or very little overlap occurs between nano-crystals, due to the high concentration of

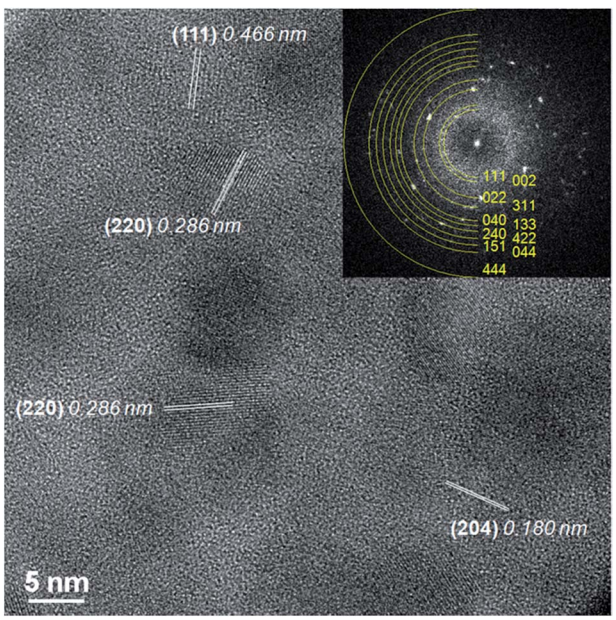

Fig. 2 Low mag HRTEM micrograph and associated Fourier transform (diffractogram): diffraction rings produced by the nano-crystallite lattice planes can be consistently indexed as the prominent reflections from the spinel phase $MgAl_2O_4$ ($Fd\bar{3}m$ with $a = 0.808$ nm).

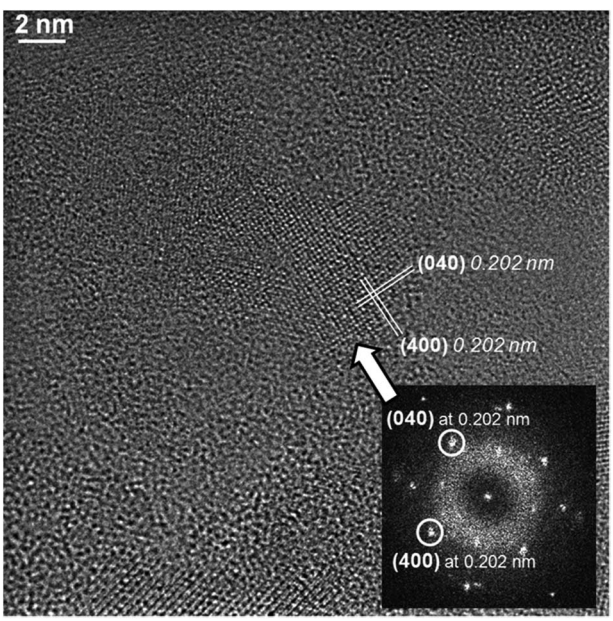

Fig. 3 Typical HRTEM image and indexed diffractogram of a nanocrystallite (arrowed). Lattice distances correspond to the usual spinel structure within a 2% accuracy.

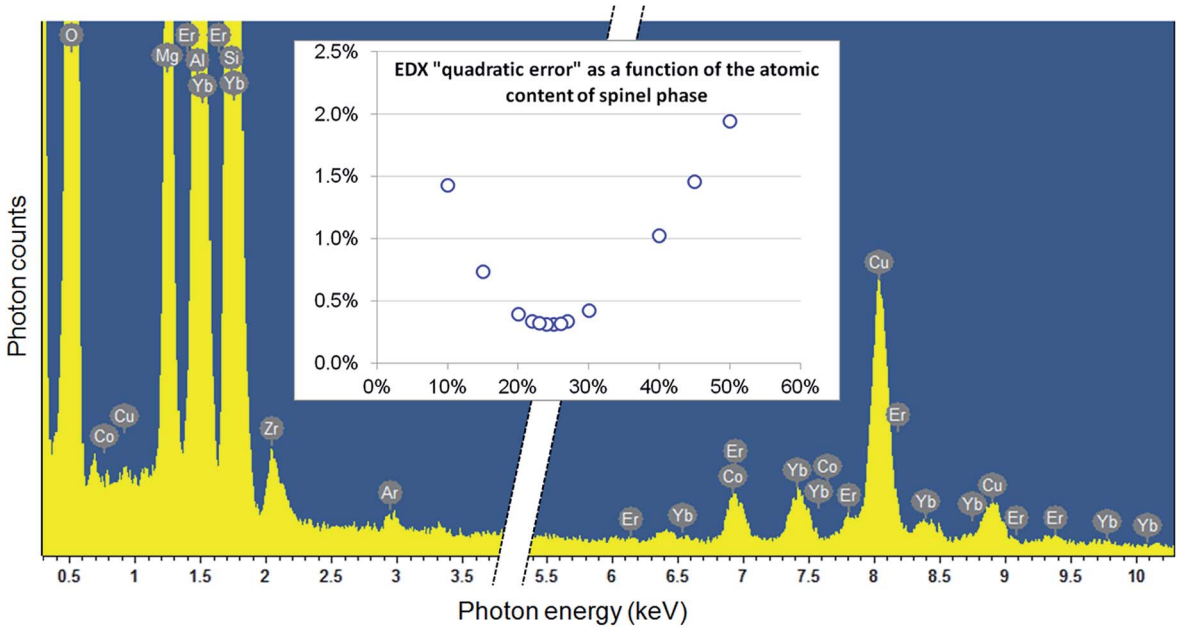

Fig. 4 Quantification of the spinel *vs.* vitreous matrix ratio: the chemical composition deduced form an EDX analysis of a large area is fitted by the following linear combination (LC): $x MgAl_2O_4 + (1 - x)SiO_2$ where x represents the atomic fraction of the spinel phase; the quadratic error defined as: $R^2 = ([O]_{LC} - [O]EDX)^2 + ([Mg]_{LC} - [Mg]_{EDX})^2 + ([Al]_{LC} - [Al]_{EDX})^2 + ([Si]_{LC} - [Si]_{EDX})^2$ presents a minimum for abound 25 at.% of the spinel phase. The detection of Zr and Ti (no shown) arises from the presence of ZrO_2 and TiO_2 constituents added in the starting compound to make the glass ceramic (they were not considered in the quantification).

nano-crystals. EDX nanoprobe analysis was performed using the classical linescan procedure as employed previously to study the distribution of Yb^{3+} ions in grains and grain boundaries in Yb^{3+}-doped YAG/Y_2O_3 ceramic bulky samples[11,12] and Yb^{3+}-doped YAG nano-ceramics[13] or Ce^{3+} ions in Ce^{3+}-doped YAG ceramic bulky samples.[14]

A typical analysis is shown in Fig. 5. As can be seen from the HREM micrograph, we have chosen here a region where a single spinel crystallite is surrounded by the glassy matrix, where no lattice fringes were resolved; 12 measurements were performed using a probe of about 3 nm, as indicated by the circle marks. The diagram on the right-hand side of Fig. 5 shows the evolution of the Yb^{3+}, Er^{3+} and Co^{2+} contents: enrichment in rare

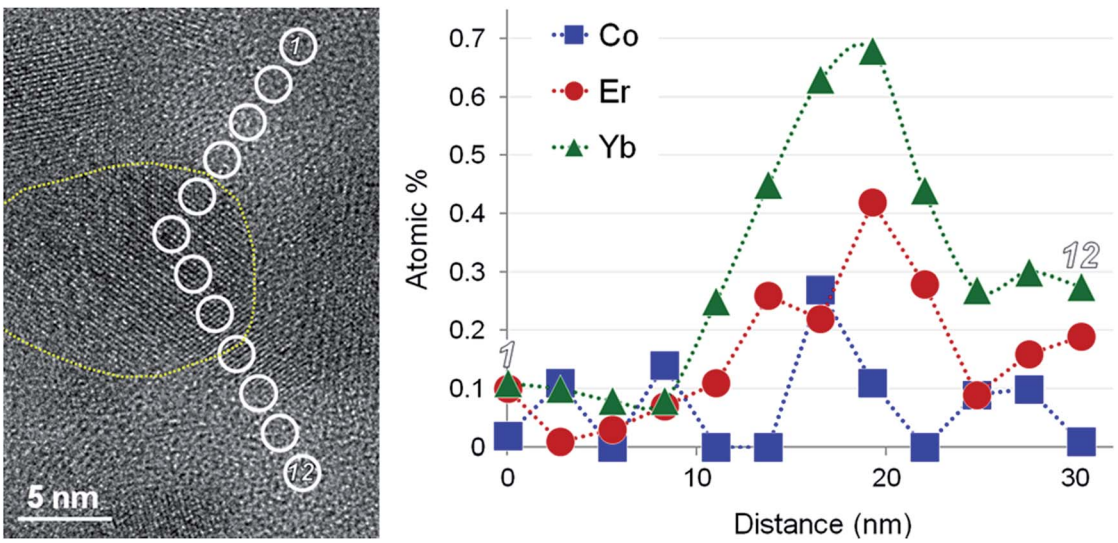

Fig. 5 Nanoprobe analysis of the distribution of the Yb, Er, and Co doping elements: 12 points have been measured across the glass matrix and a spinel particle (surrounded by a dotted line) using a probe of about 2 nm. A significant enrichment in rare earth elements is evidenced in the crystal, whereas no unambiguous conclusion can be drawn out for Co owing to the very low concentrations detected; the accuracy for all elements is about 0.2 at.%.

earth ions is clearly evidenced in the spinel phase, whereas the very low content measured for Co^{2+} does not permit any definitive conclusion about any possible distribution heterogeneity.

A large number of such EDX nano-probe measurements were performed and the results are summarized in the diagram of Fig. 6: they confirm the previous Yb^{3+} and Er^{3+} enrichment within the nano-spinel crystals as compared to the vitreous matrix. Again, the situation is less convincing regarding the very low concentration of Co^{2+} in both spinel and silica phases, but a slight enrichment of the vitreous matrix is suggested by data reported in Fig. 6.

To give a better global view of the dopant distribution, EDX elementary maps were recorded. Because of irradiation effects severely limiting the acceptable dose on the sample, it could not be possible to acquire maps with sufficient X-rays counting for an accurate quantitative treatment. However, semi-quantitative analysis gave reasonable results in agreement with the previous nano-probe data, as shown by the representative montage reported in Fig. 7.

The elemental maps for the major species (Al and Si) allow easily the $MgAl_2O_4$ spinel and the SiO_2 vitreous matrix to be separated; as already shown in Fig. 1, darker areas in STEM-HAADF images correspond to the vitreous SiO_2-based phase. These maps are treated in a quantitative way by using Aztec commercial software provided by the manufacturer of the EDX system, which means that overlap effects between X-ray lines is in principle correctly taken into account. According to this, the Yb^{3+} and Er^{3+} maps clearly confirm the greatest concentrations of Yb^{3+} and Er^{3+} dopants inside the nano-crystalline phase and only some small traces inside the SiO_2 glassy phase. Again, the Co^{2+} content appears too low on average to permit any conclusive location.

Another original worthwhile observation should be mentioned here concerning the HRTEM imaging of individual dopants. According to (i) the resolution permitted by the spherical aberration corrector, (ii) the large 'weight' (atomic number) difference between rare earth ions (Er^{3+} and Yb^{3+}) compared to the spinel and glassy phase elements (O^{2-}, Al^{3+}, Mg^{2+}, and Si^{4+}), it can be postulated that in the thinnest regions, an 'absorption-type' contrast could allow the direct visualization of heavier rare earth individual ions. In convenient so-called 'Scherzer images', atoms are expected to appear as dark dots on a brighter background, and Fig. 8a and b can be examples of such experimental evidence.

As a general conclusion of this TEM-EDX analysis, elemental maps of Fig. 7 (and, to some extent, HREM imaging in Fig. 8) confirm the results obtained from simple line scans in Fig. 5 and 6, less representative from the point of view of spatial distribution but more representative from the quantitative point of view: Er^{3+} and Yb^{3+} ions are preferentially located in the spinel nano-crystallites. This is the same conclusion for Co^{2+} ions but again the low concentration of this ion cannot permit any unambiguous location so that we need some useful help from the spectroscopic data as related in the next section. In parallel, we did not measure any significant gradient or segregation phenomenon, especially for Yb^{3+} and Er^{3+} ions, in the area of the interface between the spinel nano-crystals and the vitreous phase, although the induced damages from irradiation did not make possible to perform long acquisitions which would have been needed to gain the desirable sensitivity. This segregation was never seen for Yb^{3+} heavy ions in garnets and sesquioxides, but was encountered for example in the grain boundaries of the YAG ceramics doped with Nd^{3+} and Ce^{3+} ions.[14–17] This is an important feature for the interpretation of the Yb^{3+} double absorption line as we will discuss it later.

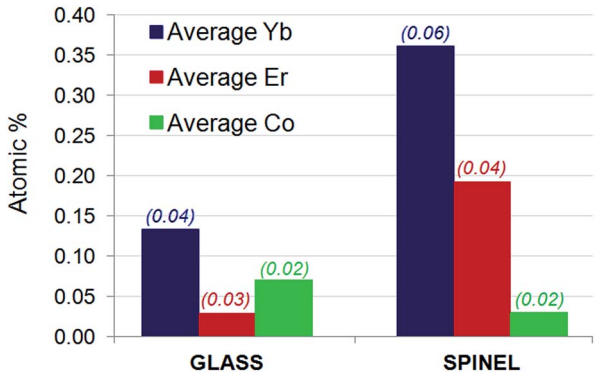

Fig. 6 Average contents measured for the doping elements Yb, Er and Co on 20 and 33 analyzed nanometric areas from the glass and spinel phases respectively; numbers in parenthesis are dispersion values.

3.3. XRD characterization

The XRD patterns of the CYE GC heat treated at 760 °C/12 h + 930 °C/4 h is presented in Fig. 9. The positions of diffused peaks closely resemble those of $MgAl_2O_4$ spinel (JCPDS, 21-1152). These peaks correspond to the reflections from the (220), (311), (400) and (440) crystal planes, respectively, of the $MgAl_2O_4$ spinel phase. The broad halo characteristics of amorphous SiO_2 matrix glass is also shown.

The diffraction peaks around 2theta = 44.8°, 36.9° and 31.3° were selected for calculating the size of $MgAl_2O_4$ nanocrystals by using Scherrer's equation. The sizes of $MgAl_2O_4$ nanocrystals are about 9.1 ± 1.3 nm for the CYE GC sample[10] in agreement with the previous STEM-HAADF results of 10 ± 0.3 nm shown in the size histogram of micrograph of Fig. 1.

3.4. Spectroscopic properties of the glass ceramics

3.4.1. Absorption spectra in the visible and the IR spectral ranges. In order to understand better the assignments of the electronic transitions we remind the energy level diagram of Er^{3+} and Yb^{3+} ions in Fig. 10.

The absorption spectra of a glass ceramic sample (noted later as GC) shown in Fig. 11a and b are composed of both sharp lines from Er^{3+} and Yb^{3+} rare earth ions and broader bands from Co^{2+} transition metal ions. We can easily see the usual Er^{3+} ion transitions from the $^4I_{15/2}$ ground state: $^4I_{15/2} \rightarrow {}^2H_{9/2}$ (~407 nm), $^4I_{15/2} \rightarrow {}^4F_{3/2}$ (442 nm), $^4I_{15/2} \rightarrow$ 4F5/2 (451 nm), $^4I_{15/2} \rightarrow {}^4F_{7/2}$ (~488 nm), $^4I_{15/2} \rightarrow {}^2H_{11/2}$ (~521 nm), $^4I_{15/2} \rightarrow {}^4S_{3/2}$ (~543 nm), $^4I_{15/2} \rightarrow {}^4F_{9/2}$ (~653 nm), $^4I_{15/2} \rightarrow {}^4I_{9/2}$ (~797 nm) (not presented here), $^4I_{15/2} \rightarrow {}^4I_{11/2}$ is hidden by $^2F_{7/2} \rightarrow {}^2F_{5/2}$ of Yb^{3+}

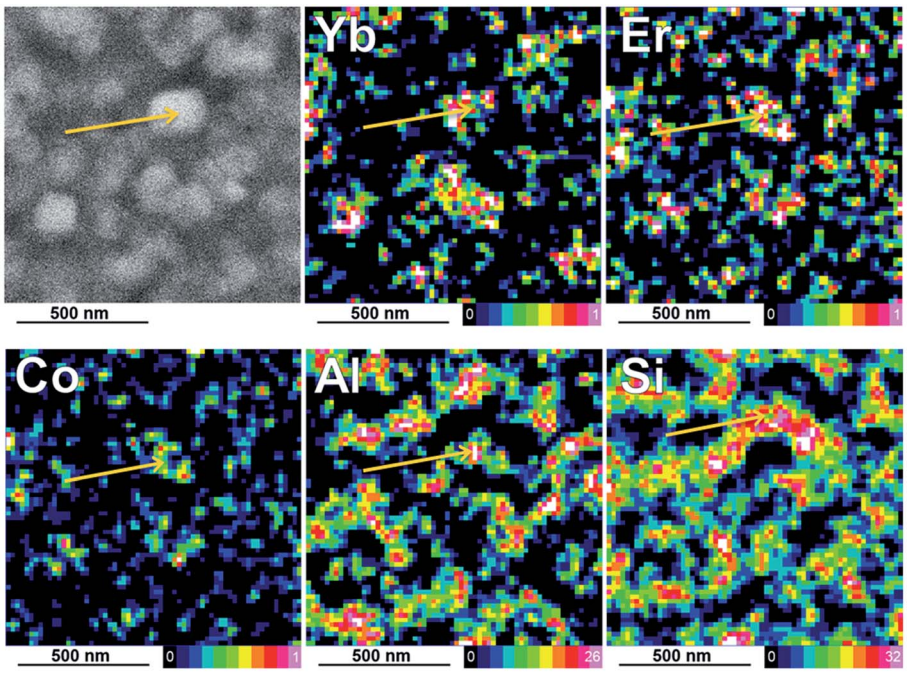

Fig. 7 Typical semi-quantitative elemental mapping of the Yb, Er, and Co dopants and the Al component of the nano-crystals and Si component of the vitreous phase; the color scale is in at.%. The arrows show the position of a nano-crystal and the same nano-crystal containing Yb, Er, and Co dopants and Al of the spinel phase. At last we show the Si element of silica glass around this nano-crystal.

ions which have much higher absorption strength (965–985 nm) and $^4I_{15/2} \rightarrow {}^4I_{13/2}$ (1510–1540 nm), respectively.

As for Co^{2+} ions, we detect the presence within two spectral ranges by the transition of both $^4T_{1g} \rightarrow {}^4T_{1g}(^4P)$ (expected O_h symmetry of glass) and $^2A_1I^2T_2(^2G) + {}^4T_1(^4P) + {}^2E^2T_1(^2G)$ (T_d

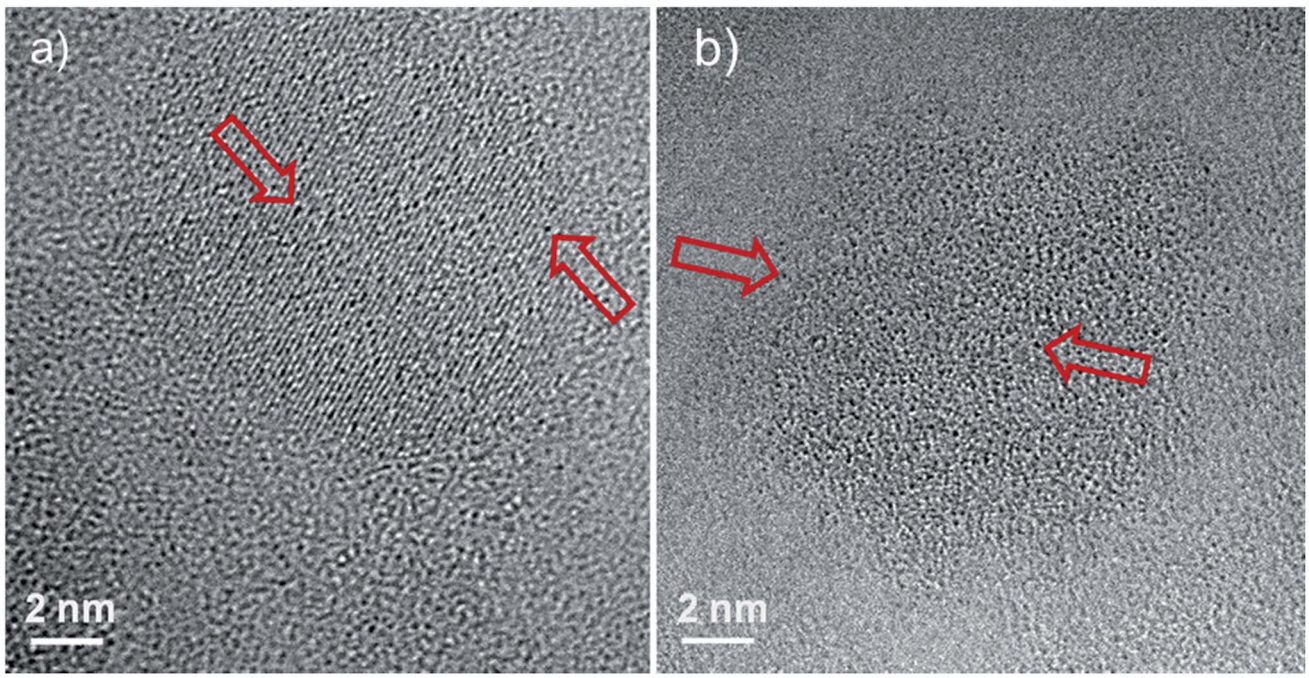

Fig. 8 Atomic resolution imaging of heavy rare earth elements in the spinel phase. (a) Typical area showing a spinel nanoparticle with a set of resolved lattice planes: note darker dots (arrows) mainly distributed in the crystalline region, and not in the surrounding vitreous matrix. (b) Similar spinel nanoparticle seen "of axis": darker atomic dots (arrows) are even more visible in the absence of lattice fringes contrast. Although the particle may have been slightly irradiated under the electron beam, no such dark dots are visible in the surrounding vitreous matrix.

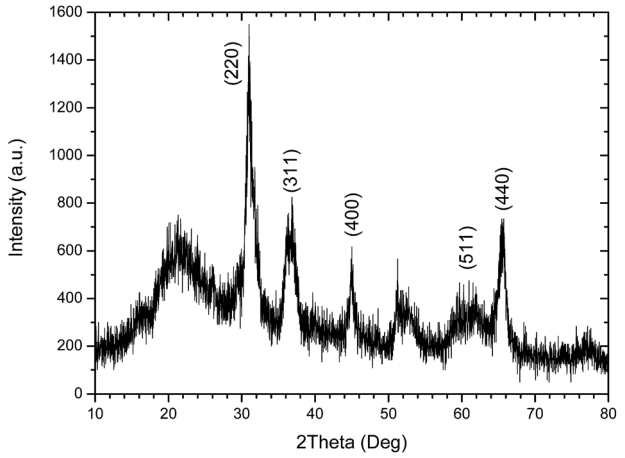

Fig. 9 XRD patterns of the CYE glass-ceramics heat treated at 760 °C/12 h + 930 °C/4 h.

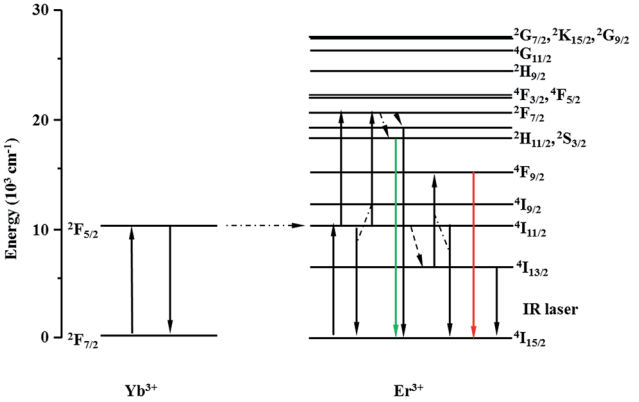

Fig. 10 Energy level diagram of Yb^{3+} and Er^{3+} ions in materials. The main absorption, emission (solid vertical arrows) and non-radiative transitions (dash vertical arrows) are mentioned. The horizontal dash arrow shows the energy transfer between Yb^{3+} and Er^{3+} ions.

Co^{2+}) (expected T_d symmetry of Mg^{2+} site in $MgAl_2O_4$ nano-spinels) between 500 and 680 nm and, in the near IR, between 1100 and 1700 nm, mainly by the $^4A_2 \rightarrow {}^4T_1(^4F)$ (T_d Co^{2+}) of the T_d symmetry in nano-spinels. This superposition of the two types of transitions justify the potentiality of this GC composition as saturable absorbers since the Co^{2+} broad absorption overlaps widely the expected laser emission from the Er^{3+} emission near 1550 nm. It has been already shown that this sample possesses excellent transparency up to nearly 87% at the near-infrared band.[10]

If, in the previous paper,[10] the question on the location of Yb^{3+} and Er^{3+} rare earth ions as dopants in the glass-ceramic from spectroscopic data has not been unambiguously solved, the assignment of Co^{2+} ions was clearly established mainly in the $MgAl_2O_4$ spinel nano-crystals. We show in Fig. 12a the weak Co^{2+} near infrared absorption as mentioned by the spectrum 3, the intensity difference of the spectrum 1 of Co^{2+} ions in the glassy phase of Co^{2+}–Yb^{3+}–Er^{3+}-doped silicate glass (CYE glass) and the spectrum 2 of Yb^{3+}–Er^{3+}-doped silicate glass (YE glass). The strongest absorption of Co^{2+} ions as observed in Fig. 12b by the spectrum 6, the intensity difference between 4 and 5 spectra, is assigned to Co^{2+} into Mg^{2+} sites of T_d symmetry in Co^{2+}–Yb^{3+}–Er^{3+}-doped $MgAl_2O_4$ nano-crystals of the (CYE GC) glass ceramics.

Let us remind that Co^{2+} ion optical transitions belong to transition metal ions with high oscillator strength ($f \sim 10^{-2}$) and high absorption cross-section in crystals is much easier to detect than rare earth ions which are characterized by much smaller $f \sim 10^{-6}$. Consequently, Co^{2+} ions can be seen at low concentration as it has been described here.

3.4.2. Observation of a new absorption line in the absorption spectra only in glass-ceramics and assignments of Yb^{3+} ions in the SiO_2 glass and the $MgAl_2O_4$ nano-crystallite phases. The previous analysis of TEM-EDX experiments indicates that we should expect the optical transitions of the three dopants in both the SiO_2 glassy phase and the $MgAl_2O_4$ nano-crystallite phase.

We will report now that spectroscopic data bring new results for these glass ceramic samples. It was found out in the absorption spectra the appearance of a new absorption line between 4 K and room temperature near 970 nm, so that it was necessary to compare the absorption of different samples containing different concentrations of Yb^{3+} and Er^{3+} ions in the two hosts of glasses and glass ceramics. First we have pointed out the double structure of the Yb^{3+} ions between 965 and 985 nm by two broad lines of practically similar intensity, so-called 0-phonon lines, with a maximum at 970 and 975.5 nm, respectively, as seen in Fig. 11b. Previously only one peak at 977 nm was observed. These two broad lines characterize the $^2F_{7/2} \rightarrow {}^2F_{5/2}$ transitions of Yb^{3+} ions between the lowest Stark energy level of each $^2F_{7/2}$ and $^2F_{5/2}$ manifolds rather than those of Er^{3+} ions, due to the much larger absorption coefficient of Yb^{3+} ions.

Concentration dependences of the Yb^{3+} absorption spectra of both glasses and glass ceramics samples containing the same amounts of Yb^{3+} and Er^{3+} rare earth ions are shown in Fig. 13a and b. Absorption spectra intensities presented for both glasses and GC are dependent on the increasing Yb^{3+} concentration. One can see the $^2F_{7/2}$ (1) $\rightarrow$ $^2F_{5/2}$ (5) double broad lines of Yb^{3+} ions with maxima at 969.5 and 975.6 nm usually associated with 0-phonon lines. The Lorentzian curves were fitted as shown in Fig. 14 and their parameters are listed in Table 1. Absorption spectra of Yb^{3+}-doped GC exhibit an evolution of the new line at 969.5 nm with respect to the line at 975.6 nm and on the other hand a higher degree of structuration than the glass spectra. By comparing these absorption spectra one can assume that the line at 975.6 nm in GC has the same glassy origin as that in glass samples with a maximum at 975.5 nm. The area values in Table 1 show that the Yb^{3+} relative population of the line at 969.5 nm is strongly increasing when the Yb^{3+} concentration increases. The absorption spectra in the GC sample have a more complex structure. It might be due to the presence of a double phase, like for example, the glassy one as already interpreted and maybe the nano-spinel crystalline phase, but this hypothesis has to be discussed.

It is interesting to compare the spectra of Yb^{3+}-doped silica glass with those we obtained recently for Yb^{3+}-doped calcium

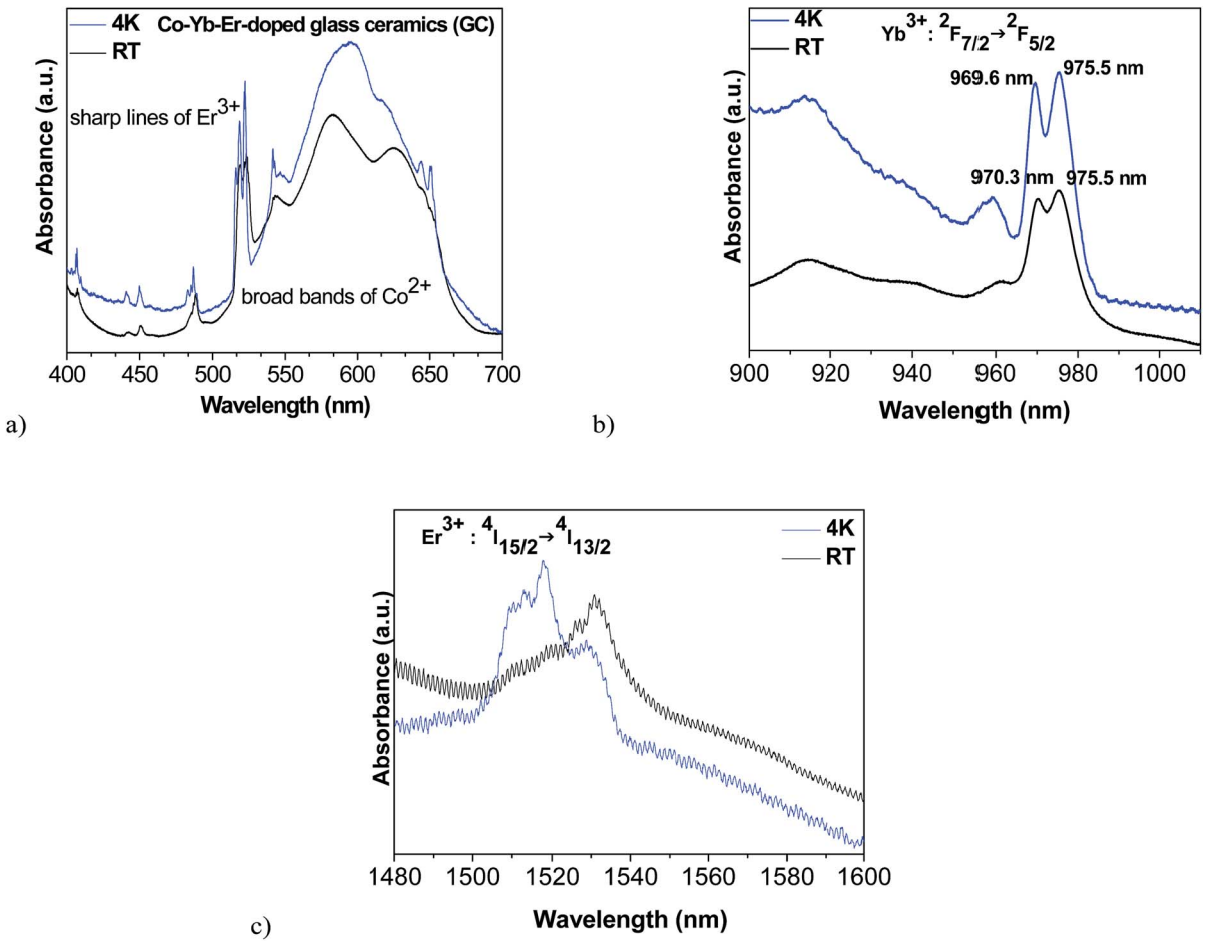

Fig. 11 Main absorption spectral regions of Co–Yb–Er-doped glass ceramics (GC) at RT and 4 K in the visible and the near IR.

alumino-silicate glasses (CAS and LSCAS) for excitation and emission spectra.[18] The spectra in these glasses are much more resolved than that of Yb^{3+}-doped silica glass, showing distinctive three $^2F_{7/2} \rightarrow {}^2F_{5/2}$ components of the absorption spectra and four $^2F_{5/2} \rightarrow {}^2F_{7/2}$ components of the emission spectra, as expected. The main reason of this difference between the two types of glasses is the presence of Ca^{2+} and Al^{3+} cations in the glass network of CAS and LSCAS which contribute to the increase of the site symmetry inside the glassy phase. The Yb^{3+} 0-phonon line in CAS and LSCAS glasses is located at 977 nm, very close to the 975.5 nm in the silica glass of the GC, and

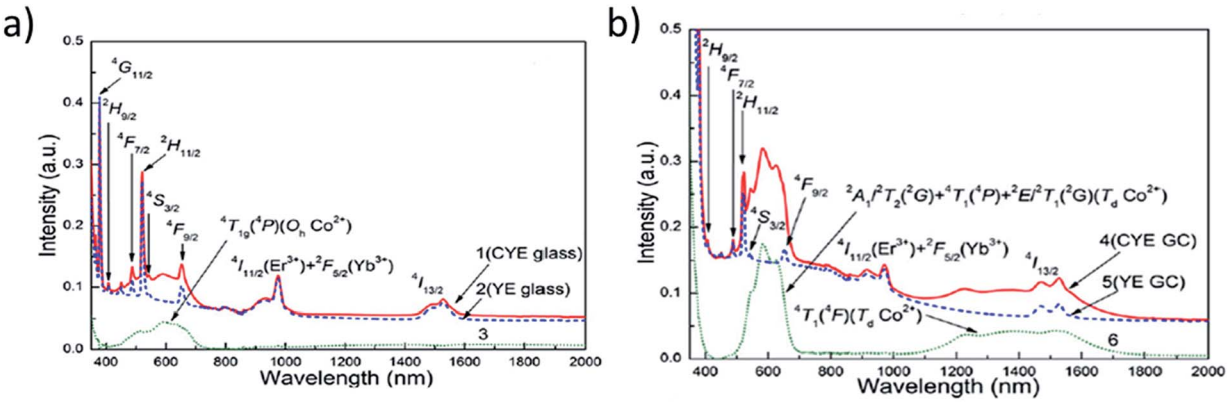

Fig. 12 (a) Absorption of Co^{2+} ions in the Co–Yb–Er-doped silicate glass (CYE glass) sample with respect to Yb–Er-doped silicate glass (YE glass), (b) absorption of Co^{2+} ions into Mg^{2+} sites of Co–Yb–Er-doped $MgAl_2O_4$ nano-crystals of the (CYE GC) glass ceramic sample.[10]

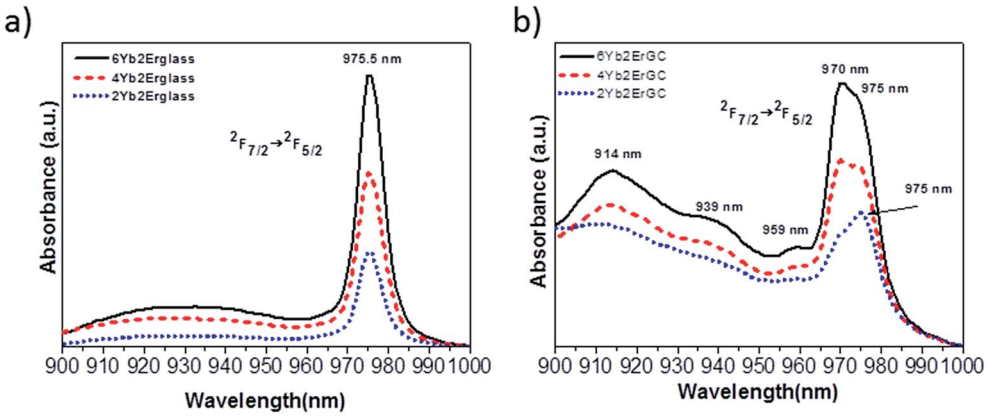

Fig. 13 Comparative detailed absorption spectra between 900 and 1000 nm of Yb^{3+} ions in glass (a) and glass ceramic (GC), (b) samples at RT.

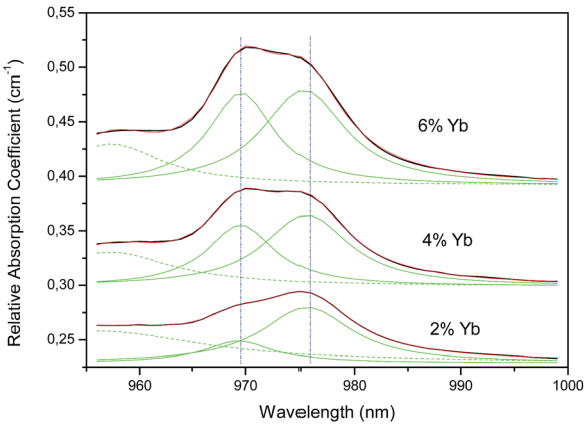

Fig. 14 Decomposition of the two 0-phonon absorption lines of Fig. 11b between 960 and 990 nm into Lorentzian curves (see Table 1).

Table 1 Parameters of the Lorentzian functions used to fit the absorption spectra

Sample	Area	Center (nm)	Half-width (nm)	Height
2% Yb	0.255	969.4	8	0.02
	0.803	975.6	10.02	0.051
4% Yb	0.677	969.5	7.66	0.056
	0.968	975.6	9.46	0.065
6% Yb	0.998	969.6	7.48	0.085
	1.263	975.4	9.22	0.087

consequently this is another proof of the assignment of the 975.5 nm peak to the silica glass phase in the GC sample.

Since the GC sample is composed of both the silicate phase and the nano-spinel crystalline phase, we also need some comparison with the rare earth-doped spinel nano-crystalline phase. We have recently published the concentration dependences of the absorption spectra and the emission spectra of Yb^{3+}-doped $MgAl_2O_4$ spinel nano-crystals in the range of 10–30 nm size, prepared by the sol–gel method and characterized by both structural and spectroscopic properties.[19]

The first striking feature is the overlapping between the Yb^{3+} 0-phonon absorption line in the silica glass at 975.5 nm and the 0-phonon line of Yb^{3+}-doped $MgAl_2O_4$ spinel nano-crystals at 976 nm (Fig. 15). Both of these two lines are very broad. In glasses this is due to the un-equivalent Yb^{3+} sites as usually expected in disordered amorphous materials and in $MgAl_2O_4$ spinel nano-crystals this is due to the following anti-site phenomenon:

$$MgAl_2O_4 \rightarrow (Mg_{1-2x}Al_{2x})[Mg_{2x}Al_{2-2x}]O_4$$

Indeed, some Al^{3+} and Mg^{2+} cations are exchanged between the cation sublattices forming pairs of anti-site defects and thus a degree of inversion is created. This degree of inversion x ranges from almost 0 for the normal spinel up to 0.5 for the inverse spinel structure. Apparently, in the spinel nano-crystal phase in ref. 19 the unresolved Yb^{3+} components indicate a large inverse spinel as a result of the multiplicity of Yb^{3+} sites observed either in octahedral or tetrahedral positions. Another effect increases the disorder by the substitution of Mg^{2+} cations. The compensation effect imposes to substitute three Mg^{2+} cations by two Yb^{3+} luminescent cations, creating one vacancy, pairs and aggregates even if the ionic radii of Yb^{3+} (85.8 pm) are much larger than those of Mg^{2+} (65 pm) and Al^{3+} (50 pm).[19] This substitution was also proposed for the Yb^{3+}–Er^{3+}-co-doped $MgAl_2O_4$ phosphor powders prepared by the combustion method.[20] In addition, other perturbed Yb^{3+} ions exist due to the morphology of the surface of the grains in contrast with the regular structure of the internal grain. It means that there are several reasons to increase disorder in the spinel lattice and to observe large broadening of both absorption and emission spectra.

As a result, in the GC samples the line located at 975 nm can be assigned to the $^2F_{7/2}$ (1) → $^2F_{5/2}$ (5) transition of Yb^{3+} ions in the glassy phase and also superposed with Yb^{3+} ions in the $MgAl_2O_4$ spinel nano-crystalline phase. There is a surprising situation, adding difficulties for the final interpretation, never

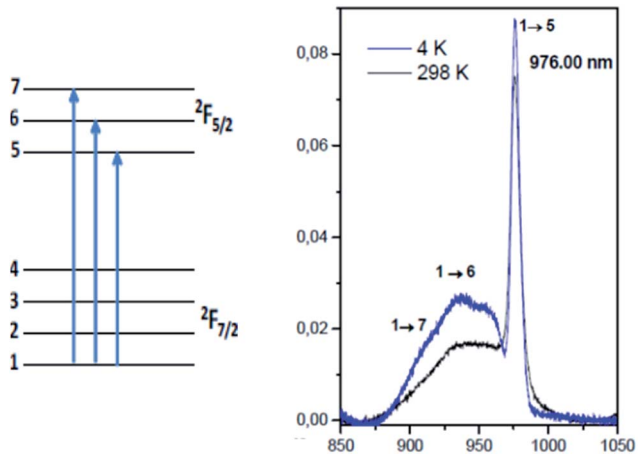

Fig. 15 Temperature dependence of absorption spectra of Yb^{3+}-doped $MgAl_2O_4$ spinel nanocrystals prepared by the sol–gel method.[19]

reported, with two Yb^{3+}-doped phases, one with SiO_2 glass, another one with $MgAl_2O_4$ nano-crystalline, which show Yb^{3+} lines in coincidence. At last we need to find new data to interpret the absorption line at 970 nm.

3.4.3. The feasibility of the laser system. We would like to bring additional results to our detailed absorption analysis by looking at the luminescence spectra and decays with the objective to check the feasibility of the laser system with the hope to get new characterization for the assignment of the origin of the unexpected 970 nm absorption line in the GC sample.

Yb^{3+} and Er^{3+} emission spectra of the GC sample recorded at RT under laser excitation at 930 nm can be seen in Fig. 16. The spectra present the emission lines corresponding to the $^2F_{5/2} \rightarrow {}^2F_{7/2}$ transitions of the Yb^{3+} ions and the $^4I_{13/2} \rightarrow {}^4I_{15/2}$ transitions of the Er^{3+} ions of interest for the laser output. The Yb^{3+} 0-phonon line at around 977 nm should be used as the pumping line of the laser diode for the energy transfer giving Er^{3+} emission within the near IR (1450–1600 nm).

Fig. 17 shows the increase of the luminescence intensity (I) of Er^{3+} $^4I_{13/2} \rightarrow {}^4I_{15/2}$ transition with the increase of 977 nm pump power (P). As it is very well known, the emission processes are complex for Er^{3+} ions and are the result of both down and up-conversion transitions due to radiative and non-radiative energy transfers between Er^{3+} ions. Consequently, the pump power dependence of the Er^{3+} near an IR emission intensity at 1550 nm under excitation at 977 nm should convey this complex process. The slope (n) of $I = P^n$ is 0.63, and not unity, which is calculated by linear fitting of dependence of the logarithms of the intensity (I) on the pump power (P).

The evidence of up-conversion processes between Yb^{3+} and Er^{3+} ions is given in Fig. 18. Up-conversion visible emission lines at 525 nm and 550 nm (green), and 660 nm (red) are clearly observed under Yb^{3+} 0-phonon line excitation at 977 nm.

The blue emission at 410 nm is also observed with a very low intensity due to an additional absorption step by up-conversion. By using the energy level diagram in Fig. 18, the emission lines at 410, 525, 560, and 660 nm are attributed to the transitions

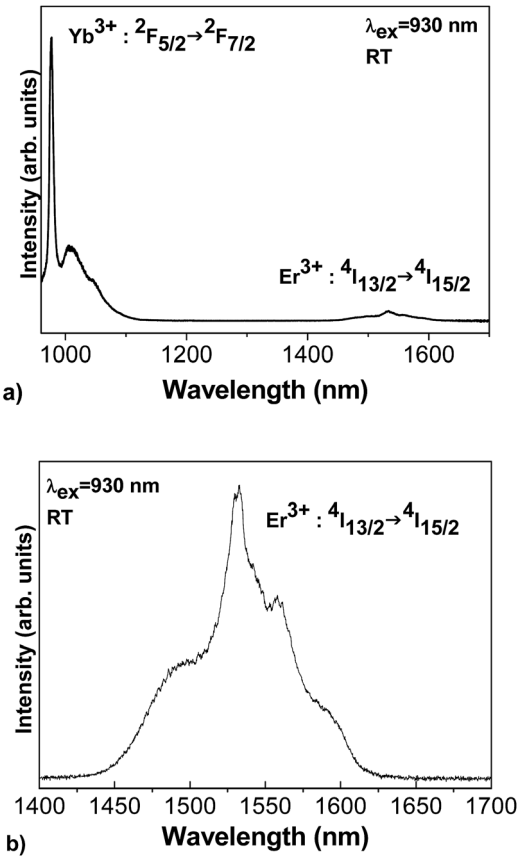

Fig. 16 (a) Yb^{3+} and Er^{3+} emission spectra of the GC sample under 930 nm laser excitation at RT. (b) Detailed Er^{3+} emission spectra of the $^4I_{13/2} \rightarrow {}^4I_{15/2}$ transition in the spectral range of the expected laser output under 930 nm laser excitation at RT.

from $^2H_{9/2}$, $^2H_{11/2}$, $^4S_{3/2}$, and $^4F_{9/2}$ excited states to the $^4I_{15/2}$ ground state of Er^{3+} ions, respectively. The green and red spectral ranges have comparable intensities as those already observed in oxide compounds depending of the values of the gap energy between Er^{3+} ion levels and the average maximum phonon energy of the host material which is the most critical factor affecting the multi-phonon relaxation in the host material. The lower is the maximum phonon energy, the smaller are the non-radiative rates.

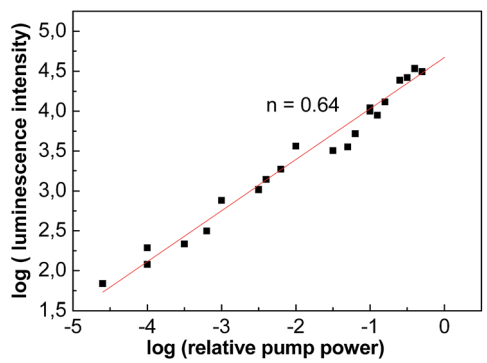

Fig. 17 Pump power dependence at 977 nm of Er^{3+} near IR emission intensity at 1550 nm.

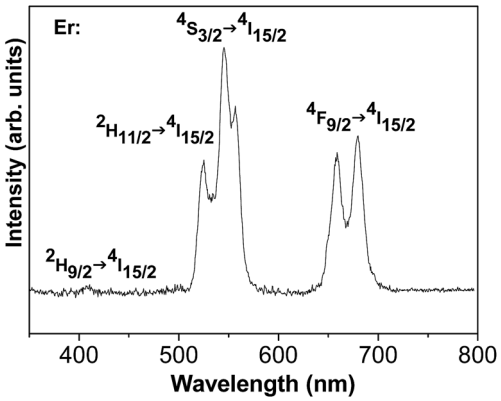

Fig. 18 Up-conversion luminescence of the Er^{3+} ions in the visible under Yb^{3+} 0-phonon line excitation at 977 nm.

The decays of both Yb^{3+} and Er^{3+} ions are seen in Fig. 19. The non-exponential profiles show the complexity of the energy transfer and the presence of multi-sites in the glassy phase and the spinel crystalline phase. The conversion energy between Yb^{3+} and Er^{3+} ions is clearly seen in Fig. 19c, by the initial rise time of the Er^{3+} $^4I_{13/2}$ energy level after Yb^{3+} pumping, with a maximum at 0.2 ms in the decay curves.

At last, let us remind that the superposition of the Co^{2+} absorption and the Er^{3+} emission around 1550 nm justifies the potential of this GC composition as saturable absorbers.[10]

3.4.4. Site selective spectroscopy as a contribution to the assignment of the new Yb^{3+} center. Site selective laser excitation within the range 880–950 nm of Yb^{3+} ions into the two highest excited levels of the $^2F_{7/2} \rightarrow {}^2F_{5/2}$ transitions of GC can be observed in Fig. 20 for 77 K.

Different excitations of the Ti-sapphire laser pump are mentioned. The absorption spectrum of the sample at 4 K, almost the same as at RT, is indicated in blue as a reference. The first obvious feature is the absence of luminescence emission of Yb^{3+} ions characterized by the 0-phonon line at 970 nm. Only the Yb^{3+} 0-phonon lines around 977 nm associated to both SiO_2 glass and $MgAl_2O_4$ nano-crystal phases are the emitting centers shifted as expected from multi-sites in glass ceramics. In addition we have not detected any energy transfer between the two centers responsible for these two broad absorption lines at 970 and 977 nm, respectively.

In Fig. 21, the site selective laser excitation at 77 K has been applied especially into the two broad $^2F_{7/2}$ (1) $\rightarrow$ $^2F_{5/2}$ (5) 0-phonon lines of Yb^{3+} ions which were detected in absorption with maxima at around 970 nm and 975 nm. Then, the different excitations are now in the range 966–980 nm. In red and black lines are reported the $^2F_{5/2}$ (5) $\rightarrow$ $^2F_{7/2}$ (1, 2, 3, 4) emission spectra under excitation at 966 nm and 969 nm, respectively, into the new absorption peak present in the GC. In green, dark blue and brown colors are reported the $^2F_{5/2}$ (5) $\rightarrow$ $^2F_{7/2}$ (1, 2, 3, 4) emission spectra under excitation at 974.8 nm, 975.8 nm and 977.8 nm, respectively, into the absorption peak already observed with the glassy phase. We confirm that only the Yb^{3+} lowest energy peak at 976 nm is giving radiative transitions. We see clearly the resolved Yb^{3+} emission spectra only under excitation at around 976 nm. A very weak emission is recorded under excitation at around 970 nm, due indeed to the excitation

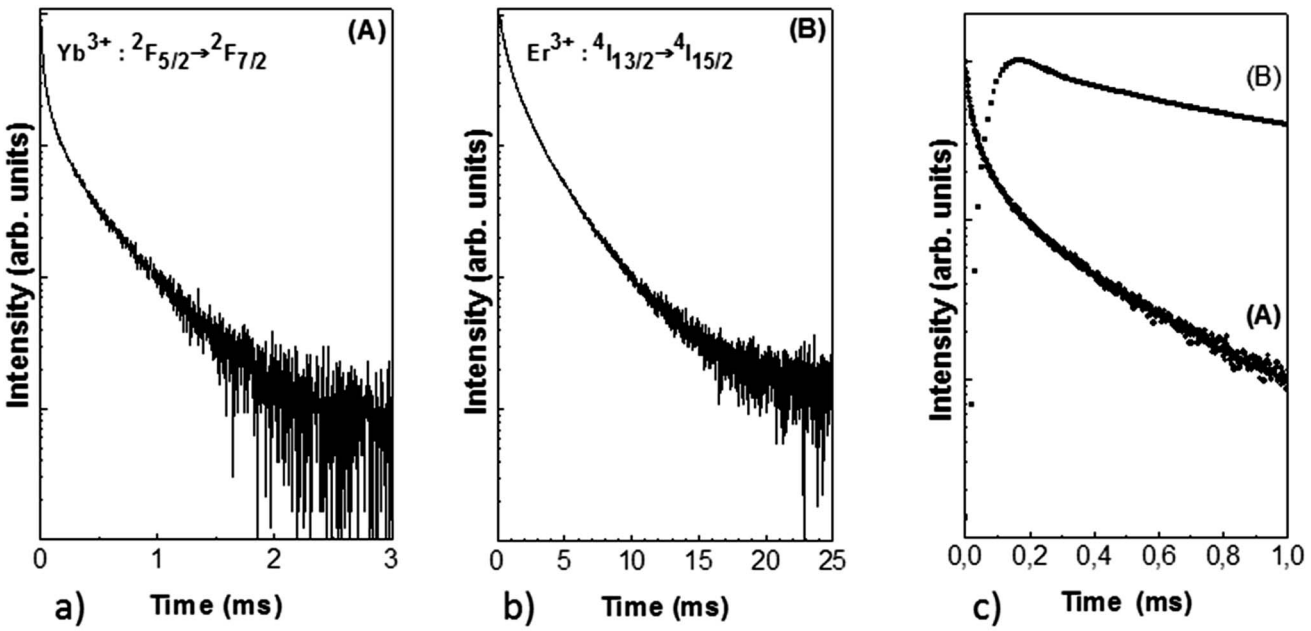

Fig. 19 Evidence of the energy transfer between Yb^{3+} and Er^{3+} ions of the GC sample. (a) Decay (A) within 3 ms of the Yb^{3+} $^2F_{5/2}$ lowest Stark excited state under excitation into the highest Stark excited state at 940 nm. (b) Decay (B) within 25 ms of the Er^{3+} $^4I_{13/2}$ lowest Stark excited state under excitation of Yb^{3+} 0-phonon line at 977 nm. (c) Superposition of the first ms of both the Yb^{3+} $^2F_{5/2}$ energy level from (A) and the Er^{3+} $^4I_{13/2}$ energy level from (B). The initial rise time of the Er^{3+} $^4I_{13/2}$ energy level is 0.2 ms.

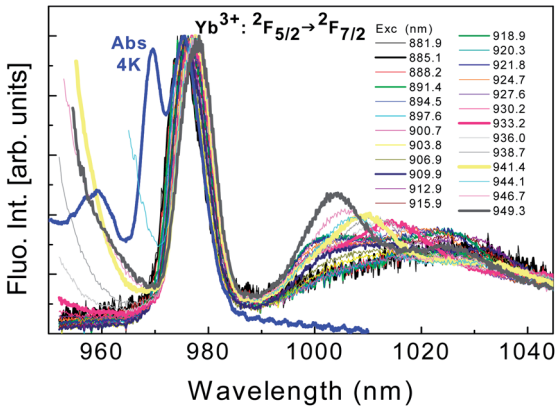

Fig. 20 Site selective laser excitation within the range 880–950 nm of Yb^{3+} ions (the two highest excited levels of the $^2F_{7/2} \rightarrow {}^2F_{5/2}$ transitions) in the glassy phase of GC at 77 K.

of the foot of the 976 nm absorption line since the overlapping of the two absorption peaks cannot be avoided.

Consequently, the Yb^{3+} center associated with the line at 970 nm is only absorbing and not emitting. It means that the Yb^{3+} resolved emission spectra observed in Fig. 21 and 22 can be associated only to pumping of the broad line at around 976 nm and reflect the superposition of the glass and the nano-spinel crystalline phases with higher intensity of Yb^{3+}-doped nano-spinel crystalline due to higher population of ions. We note that unresolved emission spectra of nano-crystals prepared by the sol–gel method[19] are not similar to highly resolved spectra of GC in Fig. 20 and 21. The relative high resolution observed in Fig. 20 and 21 leads to admit a lower degree of inversion and then much less disorder inside the nano-crystallites embedded within the glass of the GC, like if the heat treatment from glass to glass ceramic was ordering completely the spinel structure in contrast to the results for Yb^{3+}-doped nano-powders reported in ref. 19.

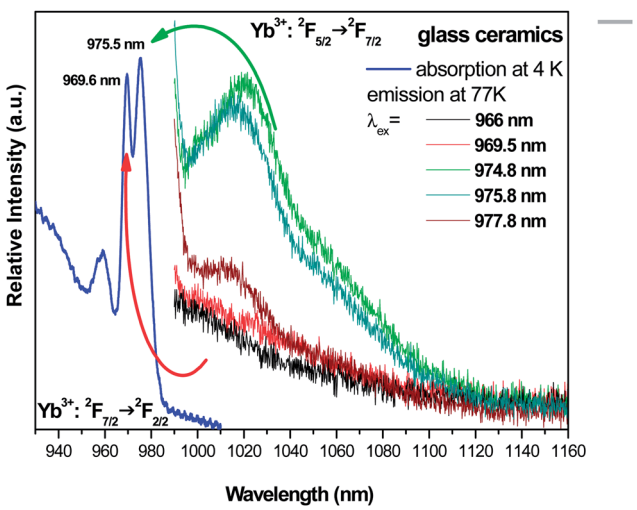

Fig. 21 Site selective laser excitation within the two broad $^2F_{7/2} \rightarrow {}^2F_{5/2}$ 0-phonon lines of Yb^{3+} ions which were detected in absorption at RT and 4 K.

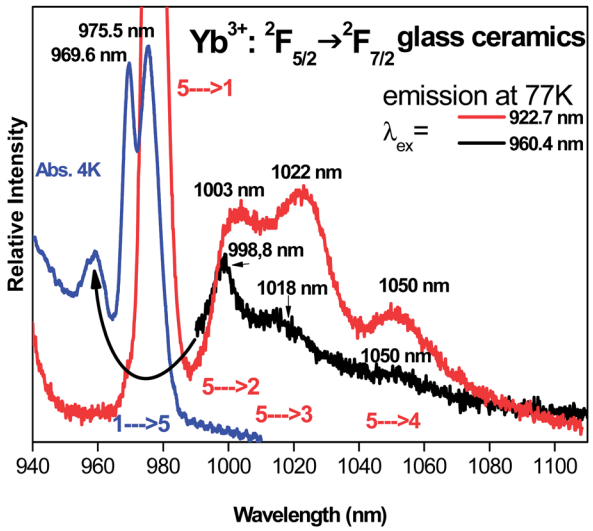

Fig. 22 Emission spectra at 77 K after excitation at 960.4 nm and 922.7 nm. In blue is reported the absorption spectrum of the sample at 4 K. An arrow is inserting to indicate the excitation position in the absorption spectrum.

Concerning the Stark components and the vibronic levels of the $^2F_{5/2}$ excited level seen in the absorption spectra of the glass-ceramics presented in Fig. 13b, unresolved in Fig. 13a in the glassy phase, we have checked in Fig. 22 the emission spectra under two pumping lines at 922.7 nm (red color) and 960.4 nm (black color), respectively. The two emission spectra are even better resolved than spectra in Fig. 20 and 21. Four components of the $^2F_{7/2}$ ground state are especially well determined at 975.5 nm, 1003 nm, 1022 nm and 1050 nm, respectively. As the strongest signals of both Yb^{3+} and Er^{3+} dopants observed by TEM-EDX were associated for spinel nano-crystals, these Yb^{3+} transitions should belong to the nano-spinel crystallites rather than the glass.

At this point of discussion, we interpret Yb^{3+} ions, and then the associated neighbor Er^{3+} ions of similar ionic radii, in both phases but with a higher population of the nano-crystalline one leading to higher fluorescence intensity and better resolution of the emission spectra. As the previous discussion on the emission properties pointed out a radiation-less Yb^{3+} center associated to the 0-phonon absorption line at 970 nm only within the GC sample, we think that this should be the result of strong perturbation acting on these centers due to the location of Yb^{3+} ions in the vicinity of the surface of the nano-crystallites. Such localization of this type of Yb^{3+} quencher ions leads to stronger distortion by the crystal field than those of the regular ions inside the grains.

Another hypothesis is the presence of Yb^{3+} aggregates at the surface of nano-crystallites so that migration of the energy by resonance between the 0-phonon lines at 970 nm might explain the quenching; however, TEM-EDX results did not detect any segregation of dopants at the interface of nano-crystal or glass and this is why we think that the probability of the formation of aggregates is very weak.

4. Conclusions

The main goal of this work was to conjugate TEM-EDX and optical spectroscopy tools, which is rather rare, for localization of Yb^{3+}, Er^{3+} and Co^{2+} dopants in a compact self-Q-switched microchip laser glass ceramics composed of $MgAl_2O_4$ spinel nano-crystals of 10–20 nm size embedded in SiO_2 glass. First of all, we have shown from spectroscopic properties that the main conditions are fulfilled for obtaining a self-Q-switched microchip laser. The previous analysis had shown that Yb^{3+} and Er^{3+} rare earth ions seem to remain in the SiO_2 glass matrix, while Co^{2+} occupy the tetrahedral sites in $MgAl_2O_4$ nano-crystals. The use of the TEM-EDX technique led to the result that Yb^{3+}, Er^{3+} and Co^{2+} dopants are located in the two phases but rather preferentially located in the spinel nano-crystallites. This important result has been clearly confirmed by the elemental mapping of Yb^{3+} and Er^{3+} rare earth ions and also by the direct visualization of these heavier rare earth individual ions. Considering Co^{2+} ions, our conclusion from absorption spectroscopy is also in favor of the location in the spinel nano-crystallites whereas TEM-EDX measurements could not be accurately applied due to the very low Co^{2+} concentration. This dopant characterization is worthwhile to be analyzed as a special case where characterization of rare earth and transition metal ions needs the association of both, TEM-EDX and optical spectroscopy tools.

In addition, there is no any significant gradient or segregation phenomenon of Yb^{3+} ions in the area of the interface between the spinel nano-crystals and the vitreous phase. Consequently, aggregates cannot be the main reason of the quenching mechanism as met with the new radiationless Yb^{3+} center pointed out by the presence of an absorption line at 970 nm of comparable intensity with that of the regular Yb^{3+} ions inside the grains of the spinel structure. The other Yb^{3+} ions localized either in the SiO_2 glass or in the $MgAl_2O_4$ spinel nano-crystalline are surprisingly emitting at almost the same wavelength, around 977 nm with the characteristic of the greatest population coming from the spinel nano-crystalline phase. The most probable assignment of this new radiationless center is to be localized on the strongly perturbed area of the nano-crystallite surface.

This characterization was only made for few samples after checking the feasibility of this compact self-Q-switched microchip laser glass ceramics. Undoubtedly, optimization of Yb^{3+}, Er^{3+} and Co^{2+} concentrations is expected in this glass ceramics before any development.

Acknowledgements

We are grateful to the CLYM (Centre Lyonnais de Microscopie, http://www.clym.fr) for its guidance in the Ly-EtTEM (Lyon Environmental tomographic TEM) project, which was financially supported by the CNRS, The Région Rhône-Alpes, The 'Greater Lyon' and the French Ministry of Research and Higher Education. We wish to warmly thank the Faculty of Chemistry of the University of Wroclaw for the access of low temperature absorption measurements.

Notes and references

1 Y. Kalisky, O. Kalisky and M. R. Kokta, *Materials*, 2008, **30**, 1775.
2 Y. Kalisky, A. Ben Amar-Baranga, Y. Shimony and M. R. Kokta, *Opt. Mater.*, 1997, **8**, 129.
3 Y. Kalisky, A. Ben-Amar Baranga, Y. Shimony, Z. Burshtein, S. A. Pollack and M. Kokta, *Opt. Mater.*, 1996, **6**, 275.
4 Y. Kalisky, in *Progress in Quantum Electronics*, ed. R. Scheps and T. Landsberg, 2004, vol. 28, p. 249.
5 W. Chen and G. Boulon, *Opt. Mater.*, 2003, **24**, 163–168.
6 R. D. Stultz, M. B. Camargo and M. Birnbaum, *OSA Proc. Adv. Solid-State Lasers*, 1995, **24**, 460.
7 K. V. Yumashev, L. A. Denisov, N. N. Posonov, N. V. Kuleshov and R. Moncorge, *J. Alloys Compd.*, 2002, **341**, 366.
8 P. Li, Y. Li, Y. Sun, X. Hou, H. Zhang and J. Wang, *Opt. Express*, 2006, **14**, 7730.
9 X. L. Duan, D. R. Yuan, X. F. Cheng, Z. M. Wang, Z. H. Sun, C. N. Luan, D. Xu and M. K. Lv, *Opt. Mater.*, 2004, **25**, 65.
10 L. Chen, C. Yu, L. Hu and W. Chen, *Solid State Sci.*, 2012, **14**, 287.
11 T. Epicier, G. Boulon, W. Zhao, M. Guzik, B. Jiang, A. Ikesue and L. Esposito, *J. Mater. Chem.*, 2012, **22**, 18221.
12 L. Esposito, M. Serantoni, A. Piancastelli, T. Epicier, D. Alderighi, A. Pirri, G. Toci, M. Vannini, S. Anghel and G. Boulon, *J. Eur. Cer. Soc.*, 2012, **32**, 2273.
13 G. Boulon, Y. Guyot, M. Guzik, T. Epicier, P. Gluchowski, D. Hreniak and W. Strek, *J. Phys. Chem. C*, 2014, **118**, 15474–15486.
14 W. Zhao, S. Anghel, C. Mancini, D. Amans, G. Boulon, T. Epicier, Y. Shi, X. Q. Feng, Y. B. Pan, V. Chani and A. Yoshikawa, *Opt. Mater.*, 2011, **33**, 684.
15 M. O. Ramirez, J. Wisdom, H. Li, Y. L. Aung, J. Stitt, G. L. Messing, V. Dierolf, Z. Liu, A. Ikesue and R. L. Byer, *Opt. Express*, 2008, **16**, 5965.
16 W. Zhao, C. Mancini, D. Amans, G. Boulon, T. Epicier, Y. Min, H. Yagi, T. Yanagitani, T. Yanagida and A. Yoshikawa, *Jpn. J. Appl. Phys.*, 2010, **49**, 022602.
17 W. Zhao, S. Anghel, C. Mancini, D. Amans, G. Boulon, T. Epicier, Y. Shi, X. Q. Feng, Y. B. Pan, V. Chani, *et al.*, *Opt. Mater.*, 2011, **33**, 68400.
18 Y. Guyot, A. Steimacher, M. P. Belançon, A. N. Medina, L. Baesso, S. Lima, L. H. C. Andrade, A. Brenier, A. M. Jurdyc and G. Boulon, *JOSA B*, 2011, **28**(10), 2510–2517.
19 R. J. Wiglusz, G. Boulon, Y. Guyot, M. Guzik, D. Hreniak and W. Strek, *Dalton Trans.*, 2014, **43**, 7752–7759.
20 V. Singh, V. Kumar Rai, S. Watanabe, T. K. Gundu Rao, L. Badie, I. Ledoux-Rak and Y.-D. Jho, *Appl. Phys. B*, 2012, **108**, 437.